Lattice Boltzmann method for diffusion-limited partial dissolution of fluids

Olav Aursjø*
IRIS AS, P.O. Box 8046, N-4068 Stavanger, Norway,
and Earth Sciences Division, Lawrence Berkeley National Laboratory, 1 Cyclotron Road, Berkeley, California 94720, USA

Steven R. Pride†
Earth Sciences Division, Lawrence Berkeley National Laboratory, 1 Cyclotron Road, MS 74R316C, Berkeley, California 94720, USA
(Received 2 March 2015; published 10 July 2015)

A lattice Boltzmann model for two partially miscible fluids is developed. By partially miscible we mean that, although there is a definite interfacial region separating the two fluids with a surface tension force acting at all points of the transition region, each fluid can nonetheless accept molecules from the other fluid up to a set solubility limit. We allow each fluid to diffuse into the other with the solubility and diffusivity in each fluid being input parameters. The approach is to define two regions within the fluid: one interfacial region having finite width, across which most of the concentration change occurs, and in which a surface tension force and color separation step are allowed for and one miscible fluid region where the concentration of the binary fluids follows an advection-diffusion equation and the mixture as a whole obeys the Navier-Stokes incompressible flow equations. Numerical examples are presented in which the algorithm produces results that are quantitatively compared to exact analytical results as well as qualitatively examined for their reasonableness. The model has the ability to simulate how bubbles of one fluid flow through another while dissolving their contents as well as to simulate a range of practical invasion problems such as injecting supercritical CO_2 into a porous material saturated with water for sequestration purposes.

DOI: 10.1103/PhysRevE.92.013306 PACS number(s): 47.11.−j, 47.55.D−, 47.56.+r

I. INTRODUCTION

Two fluids that come into contact to create an interface with a surface tension can also partially mix due to molecules diffusing from one fluid into the other across the interface. Such diffusive mixing occurs until both fluids are at their solubility limit with regard to molecules from the other fluid. A range of theories and simulation methods has been developed to study such partially miscible fluid systems (see, e.g., [1–9]).

Of note are methods based on the Cahn-Hilliard (or Landau) free energy [10,11]. This free energy contains a key term of the form $-k\nabla\tilde{c}\cdot\nabla\tilde{c}/2$ that was first introduced by van der Waals [2] as being responsible for a finite-thickness transition layer between the fluids and for surface tension. Here k is a constant and $\tilde{c}=(\rho_B-\rho_R)/\rho$ is the local order parameter (or color field) for the phase separation. The color field is set by the mass densities ρ_B and ρ_R of each fluid component and the total fluid density ρ. Minimization of the Cahn-Hilliard free energy produces a chemical potential $\mu=-a\tilde{c}+b\tilde{c}^3-k\nabla^2\tilde{c}$, where a, b, and k are taken to be positive. The gradient of this chemical potential produces a flux that enters into the conservation law controlling the composition of the fluid. The term involving parameter a allows for normal solute diffusion, the term involving b creates the phase separation and corresponds to an antidiffusion, and the term involving k provides stability and gives finite thickness to the transition layer. The parameters a, b, and k in the Cahn-Hilliard free energy independently set the surface tension, solubility, and interface width. By adding a cubic order-parameter term to the free energy (which corresponds to a quadratic order-parameter term in the above μ), nonsymmetric solubilities in the two phases can be allowed for. Minimization of the free energy also gives a fluid pressure tensor at any place where either the color or density has a gradient and that adds to the viscous stresses in the Navier-Stokes equations to account for surface tension.

Swift *et al.* [4] (see also [9,12]) developed a lattice Boltzmann algorithm that connects to a Cahn-Hilliard style of free energy and allows the associated phase separation, solute transport, and fluid flow to emerge in the macroscopic limit. Nadiga and Zaleski [5] also used a Cahn-Hilliard thermodynamic foundation to perform finite-difference modeling of the associated macroscopic flow and density variations of a liquid-vapor two-phase fluid.

In the present work, we develop an alternative lattice Boltzmann algorithm that is not tied to the Cahn-Hilliard formalism. This approach uses four input parameters to control the phase separation. These parameters set the two solubilities of each phase, the interfacial thickness and the surface tension. The model represents a relatively minor, but nonetheless nontrivial, change to many existing lattice Boltzmann models for either purely immiscible flow (see, e.g., [13,14] and references therein) or purely miscible advective diffusion (see, e.g., [15–18]). It corresponds to a well-defined physics of phase separation that is quite analogous to how the Cahn-Hilliard approach creates phase separation through antidiffusion. However, by working with a finite-width transition layer between the bulk phases, we only need to calculate the color field and the gradient of the color field at nodes in a limited region, in and around the transition layer. This region is always a smaller fraction of the total nodes being modeled. In contrast, a Cahn-Hilliard approach requires the color, the gradient of the color, and the Laplacian of color to be calculated at every fluid node in the system.

*olav.aursjo@iris.no
†srpride@lbl.gov

Although many lattice Boltzmann models have treated binary fluids that are totally miscible with no phase separation at equilibrium (see, e.g., [15–18]), there appear to be only two other studies not based on a Cahn-Hilliard free-energy approach that treat problems of binary fluids that are only partially miscible. Walsh and Saar [19] presented an interpolated Boltzmann boundary condition at the fluid-fluid interface that allows for surface-reaction kinetics in a two component system. Specifically, the dissolution of one fluid into another is modeled as a first-order chemical reaction occurring at the fluid-fluid interface with particles from a pure fluid on one side of the interface being transferred as solute into the binary fluid on the other side until an equilibrium concentration is attained at the interface. Treating both sides of the interface as binary fluids having different concentrations of the two species involved would require modification of the model. Chen and Zhang [20] used a similar first-order reaction at the interface between two fluids; however, their treatment does not allow the interface position to relocate as mass passes across the interface from one fluid to the other and thus does not appear capable of modeling bubble evaporation.

One motivation for the present study is the dynamics that occurs when supercritical CO_2 is injected into a porous material initially saturated with water. Such modeling has pertinence to geological sequestration of CO_2. At a temperature of 313 K and a pressure of 7 MPa, initially pure supercritical CO_2 and pure water diffuse into each other up to a solubility of about 5% ($scCO_2$ into water) and 2% (water into $scCO_2$). In the present modeling, we aim to capture the partial mixing and flow of the two fluids without including the changing surface tension [21,22] or the density changes observed when these fluids mix.

Our approach is to require the concentrations of the two fluids immediately adjacent to the fluid-fluid interfacial region to always be at their solubility limit with respect to the solute from the other fluid. The interface region is controlled to be several lattice sites or more in thickness and is modeled using a modified and altered form of the D'Ortona *et al.* [23] approach and the Latva-Kokko–Rothman [24] approach to color separation. This approach allows for both normal diffusion across the interface and an antidiffusion that creates phase separation. Surface tension is treated using the Brackbill *et al.* [25] approach of modeling surface tension as a volume force acting on the total fluid movement throughout the interfacial region. Outside the interface region, the binary fluid is purely miscible (no color separation step) with concentration obeying the advection-diffusion equation with the fixed concentrations at the edges of the interface region acting as effective boundary conditions. Fluid mass of either type may pass in either direction across the interface and the interface is allowed to freely displace during the diffusion and flow dynamics.

II. GOVERNING CONTINUUM EQUATIONS

We consider the mixing and flow dynamics of an isothermal binary fluid with composition-dependent properties. The state of the fluid mixture may be described in terms of the mass density of the mixture $\rho(\mathbf{x},t)$, the velocity field $\mathbf{u}(\mathbf{x},t)$, the pressure $p(\mathbf{x},t)$, and the concentration $\varphi(\mathbf{x},t)$ of one of the two fluids present. The concentration is here defined as the ratio of the mass density of one component to the total mass density. Using the Einstein summation convention, where Latin indices denote Cartesian spatial components, the mass conservation and the momentum conservation equations may be written, respectively, in component form as

$$\partial_t \rho + \partial_i(\rho u_i) = 0, \tag{1}$$

$$\rho(\partial_t u_i + u_j \partial_j u_i) = -\partial_i p + F_i + \partial_j \tau_{ij}, \tag{2}$$

where F_i denotes the components of any applied volume force and

$$\tau_{ij} = \rho\nu\left[\partial_i u_j + \partial_j u_i - \frac{2}{d}\partial_k u_k \delta_{ij}\right] + \xi\,\partial_k u_k \delta_{ij} \tag{3}$$

expresses the components of the viscous stress tensor for a d-dimensional system. Here ν and ξ are, respectively, the kinematic shear viscosity and the bulk (or volume) viscosity of the fluid, and δ_{ij} is the Kronecker delta. The kinematic shear viscosity ν would typically depend on the variable composition of the fluid mixture. Finally, an equation of state is required to describe the relation between the concentration and mass density and the pressure, i.e., $p(\rho,\varphi)$.

For our isothermal system, the evolution of the concentration distribution through the fluid, due to diffusion and advection, is described by the equation [26]

$$\rho(\partial_t \varphi + u_i \partial_i \varphi) = \partial_i(D_0 \rho \partial_i \varphi), \tag{4}$$

where D_0 is the diffusion coefficient of the fluid mixture and we have disregarded any possible pressure gradient inside the divergence as negligibly small. At low Mach numbers, defined by $|\mathbf{u}|/c \ll 1$, where c is the speed of sound, compressional changes in the density may be neglected and the combined fluids are required to satisfy the incompressible Navier-Stokes equations

$$\partial_i u_i = 0, \tag{5}$$

$$\rho(\partial_t u_i + u_j \partial_j u_i) = -\partial_i p + F_i + \rho\nu\partial_j\partial_j u_i, \tag{6}$$

and the advection-diffusion equation

$$\partial_t \varphi + u_i \partial_i \varphi = \partial_i(D_0 \partial_i \varphi). \tag{7}$$

III. MODEL DESCRIPTION

We consider two viscous fluids, blue and red, that possess an interfacial tension where they come into contact. Instead of being completely immiscible, the fluids are allowed to partially mix until they reach an equilibrium state where the concentration of blue fluid is α_1 in the mainly blue phase and α_2 in the mainly red phase. To reach this equilibrium state, the two fluids diffuse into each other with diffusivities D_B and D_R, where D_B is the diffusivity of blue particles in the mainly red phase and D_R is the diffusivity of red particles in the mainly blue phase.

Here a lattice Boltzmann method is developed that incorporates these features into the flow modeling. To do this, we divide the algorithm into two parts. One part describes the advection-diffusion process away from the interface between the two phases and one part describes the behavior within a finite interface region and incorporates a phase-separation process and an interfacial tension. The algorithm involves

the distribution function of the combined fluids $f_\alpha(\mathbf{x},t)$ and the distribution function for the blue fluid $g_\alpha(\mathbf{x},t)$, at lattice positions $\mathbf{x}$ and time t, where the index α denotes the various directions in which the neighboring lattice sites are located.

Let us first focus on the total distribution $f_\alpha(\mathbf{x},t)$. Introducing a lattice constant Δx and a time discretization Δt, this function evolves according to the lattice Boltzmann equation (LBE)

$$f_\alpha(\mathbf{x}+\mathbf{c}_\alpha\Delta t,t+\Delta t) = f_\alpha(\mathbf{x},t) + \Omega_\alpha^\nu(\mathbf{x},t) + \Delta f_\alpha^F(\mathbf{x},t), \quad (8)$$

where $\Delta f_\alpha^F(\mathbf{x},t)$ is the volume force term and $\Omega_\alpha^\nu(\mathbf{x},t)$ is the collision operator. We use here the Bhatnagar-Gross-Krook (BGK) collision operator

$$\Omega_\alpha^\nu(\mathbf{x},t) = \lambda_\nu\big[f_\alpha(\mathbf{x},t) - f_\alpha^{\mathrm{eq}}(\rho,\mathbf{u})\big], \quad (9)$$

where $-\Delta t/\lambda_\nu$ is the relaxation time and f_α^{eq} is the equilibrium distribution. By choosing an equilibrium distribution of the form

$$f_\alpha^{\mathrm{eq}}(\rho,\mathbf{u}) = w_\alpha\rho\left(1+\frac{c_{\alpha i}u_i}{c_S^2}+\frac{Q_{\alpha ij}u_iu_j}{2c_S^4}\right), \quad (10)$$

where w_α are the lattice weights in the various directions and c_S is a constant related to the lattice structure, the correct hydrodynamical equations may be recovered in the long-wavelength limit. Here

$$Q_{\alpha ij} = c_{\alpha i}c_{\alpha j} - c_S^2\delta_{ij}, \quad (11)$$

$c_{\alpha i}$ are the vector components of the discrete set of constant velocity vectors $\mathbf{c}_\alpha$, in the various lattice directions, and u_i are the vector components of the fluid velocity $\mathbf{u}(\mathbf{x},t)$. The force term in Eq. (8) is given as [27]

$$\Delta f_\alpha^F = w_\alpha\left(1+\frac{\lambda_\nu}{2}\right)\left[\frac{c_{\alpha i}-u_i}{c_S^2}+\frac{c_{\alpha j}u_j}{c_S^4}c_{\alpha i}\right]F_i\Delta t, \quad (12)$$

where F_i are the components of the applied volume force. Guo *et al.* showed that this form of the force term ensures the recovery of the correct hydrodynamical equations.

The total mass density of the fluid is given as

$$\rho(\mathbf{x},t) = \sum_\alpha f_\alpha(\mathbf{x},t), \quad (13)$$

while the total mass flux of the fluid mixture is here defined as

$$\rho(\mathbf{x},t)u_i(\mathbf{x},t) = \sum_\alpha f_\alpha(\mathbf{x},t)c_{\alpha i} + \frac{1}{2}F_i\Delta t. \quad (14)$$

By relating the kinematic viscosity to the relaxation parameter λ by

$$\nu = -c_S^2\left(\frac{1}{2}+\frac{1}{\lambda_\nu}\right)\Delta t \quad (15)$$

and the pressure to the mass density through an equation of state

$$p = c_S^2\rho, \quad (16)$$

the flow equations (1) and (2) are recovered in the long-wavelength limit. The details of this derivation are given in Appendixes A and B.

If the pure red and blue fluids have kinematic viscosities given as ν_{R} and ν_{B}, respectively, the partial mixing being allowed for, results in the fluid having an effective viscosity ν_{eff} at each lattice point that is different from these pure values. In our model, this is allowed for by letting the relaxation parameter λ_ν take on different values for different concentration $\varphi = \rho_{\mathrm{B}}/\rho$ of blue fluid, through the use of an effective viscosity model. For the numerical modeling presented in this paper, we choose the so-called ideal viscosity model [28,29], first proposed by Arrhenius, where

$$-c_S^2\left(\frac{1}{2}+\frac{1}{\lambda_\nu}\right)\Delta t = \nu_{\mathrm{eff}} = \nu_{\mathrm{B}}^{\varphi}\nu_{\mathrm{R}}^{(1-\varphi)}. \quad (17)$$

Other models for ν_{eff} could of course be adopted.

In the low-Mach-number regime considered here, systems where buoyancy effects are present under the influence of gravity may in this model be simulated by introducing a volume force of the form $\rho_g(\varphi)g_i$, where $\rho_g(\varphi)$ is a given analytical function of the concentration and g_i are the vector components of the gravitational acceleration. This is a valid approximation as long as the concentration dependence is negligible in the inertial acceleration of the fluid, i.e., when $|du_i/dt|/g_i \ll 1$.

In our lattice Boltzmann (LB) model, the interaction between the two fluids is described by the evolution of the distribution function $g_\alpha(\mathbf{x},t)$ of the blue fluid. This distribution function is related to the blue mass density as

$$\rho_{\mathrm{B}}(\mathbf{x},t) = \sum_\alpha g_\alpha(\mathbf{x},t). \quad (18)$$

As described in the introduction of this section, our algorithm is divided into two parts: one part for the behavior within a finite interface region (region II), where a phase segregation and an interfacial tension are incorporated, and one part for the advection-diffusion process in the bulk regions (region I), away from the fluid-fluid interface. The technical definition of the two regions will be given shortly in Sec. III A. In both our regions, the given description of the evolution of the total fluid distribution $f_\alpha(\mathbf{x},t)$ is valid. Only the applied forcing terms will differ in the two regions. The evolution of the blue fluid distribution $g_\alpha(\mathbf{x},t)$ is, however, distinctive for each separate region.

A. Region definitions

In our region II algorithm, a step that promotes phase separation needs to be included. This step, which gives the blue fluid distribution $g_\alpha(\mathbf{x}+\mathbf{c}_\alpha\Delta t,t+\Delta t)$, is in direct contradiction to the diffusive process taking place in region I. To avoid having conflicting algorithm steps applied to a single lattice site, we define our two regions, I and II, to be complementary sets of lattice sites. Region II, where a so-called recoloration scheme and the interfacial force are to be applied, is the transition zone between the two fluid phases. Remember that our algorithm aims to describe a system where the phases are allowed to diffuse through the interface between them and partially mix until they reach a concentration threshold. Thus, if we assume that the concentration at the boundary points immediately adjacent to the transition region are maintained at the solubility limits, the first condition for a lattice site to be in this transition zone is that the blue fluid

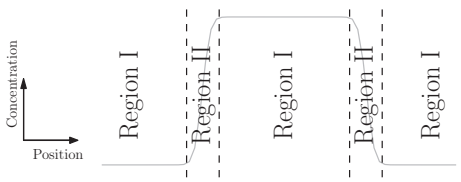

FIG. 1. Schematic representation of how the separate algorithm regions are defined. The figure shows the concentration profile of a circular blue bubble surrounded by red fluid.

concentration φ lies in the range

$$\alpha_2 \leqslant \varphi \leqslant \alpha_1, \tag{19}$$

with α_2 being the equilibrium solubility of blue in mainly red fluid and $1-\alpha_1$ being the equilibrium solubility of red in mainly blue fluid. Both α_1 and α_2 are input parameters in our algorithm.

To avoid having region II grow as adjacent lattice points in region I reach the desired fluid concentration due to the advective-diffusive mixing occurring there, it is necessary to have a second condition that also must be met for lattice points to be in region II. In order to introduce this condition we first need to define a local color difference

$$\tilde{c}(\mathbf{x},t) = \frac{\rho_{\mathrm{B}}(\mathbf{x},t) - \rho_{\mathrm{R}}(\mathbf{x},t)}{\rho(\mathbf{x},t)} = 2\varphi(\mathbf{x},t) - 1, \tag{20}$$

where $\varphi(\mathbf{x},t) = \rho_{\mathrm{B}}(\mathbf{x},t)/\rho(\mathbf{x},t)$ is the concentration of blue fluid at node $\mathbf{x}$. This is subsequently used to define a color gradient

$$\mathbf{n}(\mathbf{x},t) = \frac{1}{c_S^2 \Delta t} \sum_{\alpha} w_\alpha \tilde{c}(\mathbf{x} + \mathbf{c}_\alpha \Delta t, t)\mathbf{c}_\alpha. \tag{21}$$

A Taylor expansion of $\tilde{c}(\mathbf{x} + \mathbf{c}_\alpha \Delta t, t)$ is what allows $\mathbf{n}$ to be identified as the color gradient $\nabla\tilde{c}$. We know that the absolute value of this color gradient has its peak in the middle of the interfacial zone between the two fluids and that it decreases rapidly away from it. We also know that, during the advective-diffusive process, it can also be nonzero, but small, away from the interfacial zone. We use this to construct the second condition that must be met in region II, namely, the absolute value of the color gradient

$$|\mathbf{n}| > \bar{n}, \tag{22}$$

where $\bar{n}$ is a small but finite threshold value. It could be chosen as $\bar{n} = \epsilon[\tilde{c}]/\ell$, with ℓ being an estimate of the interface width, $[\tilde{c}] = 2(\alpha_1 - \alpha_2)$ being the total jump in the color difference across an interface, and ϵ being a small number such as 10^{-2}. Introducing such a threshold leads to a very small deviation between the intended saturation levels, given by α_1 and α_2, and the obtained equilibrium concentrations. The value used for $\bar{n}$ in our simulations results in a deviation amounting to less than 0.001% of the intended solubility levels.

Region I, where the diffusive scheme is used, is then simply the complementary set of lattice sites to that of region II. Figure 1 shows a schematic representation of where the two separate algorithm regions apply in a system composed of a circular blue fluid bubble surrounded by red fluid. Now, having properly defined the separate regions, let us again direct our focus towards the evolution steps of $g_\alpha(\mathbf{x},t)$ in the two regions.

B. Region I

In region I, our model aims to have the two fluids experience an advective-diffusive mixing. Similarly to the total fluid distribution f_α, the blue distribution g_α follows an LBE

$$g_\alpha(\mathbf{x} + \mathbf{c}_\alpha \Delta t, t + \Delta t) = g_\alpha(\mathbf{x},t) + \Omega_\alpha^D(\mathbf{x},t) + \Delta g_\alpha^F(\mathbf{x},t). \tag{23}$$

Here

$$\Omega_\alpha^D = \lambda_D\left[g_\alpha(\mathbf{x},t) - g_\alpha^{\mathrm{eq}}(\rho_{\mathrm{B}},\mathbf{u})\right], \tag{24}$$

where λ_D is related to the diffusivity of the blue fluid by

$$D_0 = -c_S^2\left(\frac{1}{2} + \frac{1}{\lambda_D}\right)\Delta t \tag{25}$$

and

$$\Delta g_\alpha^F(\mathbf{x},t) = w_\alpha\left(1 + \frac{\lambda_D}{2}\right)\frac{1}{c_S^2} c_{\alpha i} F_i \varphi \Delta t. \tag{26}$$

In the force term $\Delta g_\alpha^F(\mathbf{x},t)$, we have introduced the concentration $\varphi = \rho_{\mathrm{B}}/\rho$ of the blue fluid component. In Appendix C we show that this form of the force term ensures recovery of the desired form of the advection-diffusion equation without any unwanted terms in the continuum limit. The equilibrium distribution for the blue fluid is given as

$$g_\alpha^{\mathrm{eq}}(\rho_{\mathrm{B}},\mathbf{u}) = w_\alpha \rho_{\mathrm{B}}\left(1 + \frac{c_{\alpha i}u_i}{c_S^2} + \frac{Q_{\alpha ij}u_i u_j}{2c_S^4}\right), \tag{27}$$

where $Q_{\alpha ij}$ is given by Eq. (11). This leads to the blue fluid density obeying the advection-diffusion equation (4) in the long-wavelength limit without having any unwanted terms. We should point out that this is achieved by, in addition to introducing the forcing term, relating the distribution function g_α in a nonstandard way to the mass density ρ_{B}, rather than directly to the concentration φ (see Appendix C).

An argument similar to what holds for the viscosities also holds for how the diffusivity of blue particles changes with concentration. In the low-Mach-number limit being treated, where the total density is effectively constant from a diffusion perspective (the density variations responsible for pressure variations come in at the first order of the Mach number and may thus be ignored in the advection-diffusion equation), the mutual diffusivity of red particles through blue is the same as blue through red at any given point in the system. An effective diffusivity model for D_0 equivalent to the Arrhenius model of viscosity could be proposed. However, if modeling the diffusive mixing of supercritical CO_2 and water, the solubilities would be set to roughly $\alpha_2 = 0.05$ and $1 - \alpha_1 = 0.02$. This means that there is very little dependence of the diffusivity on the concentration on either side of the interface. In any such case involving low solubilities, it is appropriate to define a constant diffusivity of D_{R} for how red particles diffuse in the blue fluid at infinite dilution and D_{B} for how blue diffuses in red at infinite dilution. The diffusion relaxation parameter λ_D

is then selected using

$$-c_S^2\left(\frac{1}{2}+\frac{1}{\lambda_D}\right)\Delta t=\begin{cases}D_{\mathrm{B}} & \text{if } \varphi<\frac{1}{2}(\alpha_1+\alpha_2)\\ D_{\mathrm{R}} & \text{if } \varphi>\frac{1}{2}(\alpha_1+\alpha_2),\end{cases} \tag{28}$$

where $(\alpha_1+\alpha_2)/2$ defines the midpoint of the interfacial region. Another effective diffusivity model might be more appropriate if the solubilities α_2 and $1-\alpha_1$ are larger. Note here that the evolution of the blue fluid distribution g_α couples to the combined fluid distribution f_α through the velocity field $\mathbf{u}(\mathbf{x},t)$ and, in a secondary way, through the effective viscosity model.

C. Region II

In region II, our model needs to incorporate phase separation, as well as an interfacial tension, between the two fluids. This entails the use of an algorithm for immiscible fluids. When applying such an algorithm it is important to have an immiscible model where spurious interface currents [30,31] are kept small so as to reduce subsequent errors in the advection of the soluble fluid close to the fluid-fluid interface. Accordingly, we have used a model similar to those presented by Wu *et al.* [32] and Walsh and Saar [19]. These models use the gradient-based recoloration scheme originally proposed by D'Ortona *et al.* [23] and later slightly changed by Latva-Kokko and Rothman [24]. They also use a continuum volume force proposed by Brackbill *et al.* [25] for the modeling of an interfacial tension. To allow for dissolution across the interface, we modify the recoloration step proposed by Latva-Kokko and Rothman [24].

The interfacial tension is implemented as a volume force [25]

$$\mathbf{F}_{\mathrm{IT}}(\mathbf{x},t)=\sigma\kappa(\mathbf{x},t)\frac{\mathbf{n}}{[\tilde{c}]}, \tag{29}$$

where $\mathbf{n}=\nabla\tilde{c}$ is given by Eq. (21), σ is the interfacial tension, and $[\tilde{c}]$ is the overall jump in the color $\tilde{c}$ across the interfacial region. The interface curvature κ is given as

$$\kappa=-\nabla\cdot\left(\frac{\mathbf{n}}{|\mathbf{n}|}\right) \tag{30}$$

$$=-\frac{1}{|\mathbf{n}|}\left(\nabla\cdot\mathbf{n}-\frac{\mathbf{n}}{|\mathbf{n}|}\cdot\nabla|\mathbf{n}|\right). \tag{31}$$

Though Eqs. (30) and (31) are analytically identical, Brackbill *et al.* [25] showed that a finite-difference approximation to Eq. (30) has the interface curvature peaking near the edges of the interfacial region, while a finite-difference approximation to Eq. (31) produces a κ that is maximum nearer the center the interfacial region, where also the color gradient is maximum. In our model, we numerically determine the curvature using Eq. (31), since this leads to better results in practice. Advantages with this volume force implementation of surface tension include having reduced interfacial spurious currents, having a continuous pressure change across the fluid-fluid interface [32], and having the interfacial tension be given directly as an input parameter. We note in passing that if $\mathbf{n}\cdot\mathbf{F}_{\mathrm{IT}}/|\mathbf{n}|$ is integrated across the transition layer, the result is the pressure change across the interface also known as the capillary pressure.

The evolution of the blue distribution function is here given as

$$g_\alpha(\mathbf{x}+\mathbf{c}_\alpha\Delta t,t+\Delta t)=\varphi f_\alpha(\mathbf{x},t)+\frac{\varphi\Delta t}{2c_S^2}w_\alpha c_{\alpha j}F_j + \beta h_\varphi\rho w_\alpha\frac{c_{\alpha i}n_i}{|\mathbf{c}_\alpha||\mathbf{n}|}, \tag{32}$$

where β is a unitless parameter that sets the interface width [24] and n_i are the vector components of the color gradient $\mathbf{n}$. Typically, $\beta\leqslant 1$ to avoid the occurrence of negative particle distributions. We have here also introduced a unitless window function h_φ that is zero at the boundary between regions I and II and that peaks in the middle of region II with a value of $1/4$. It is defined

$$h_\varphi=\frac{(\alpha_1-\varphi)(\varphi-\alpha_2)}{(\alpha_1-\alpha_2)^2}, \tag{33}$$

which is non-negative throughout region II where $\alpha_2<\varphi<\alpha_1$. This modification to recoloration results in a blue concentration equal to α_1 on one side of the transition zone and α_2 on the other. In the recoloration scheme of Latva-Kokko and Rothman [24] $h_\varphi=\varphi(1-\varphi)$, which corresponds to perfect immiscibility in our scheme with $\alpha_1=1$ and $\alpha_2=0$.

By itself, the first term on the right-hand side of Eq. (32) results in the blue concentration obeying the standard advection-diffusion equation with a diffusivity of $c_S^2\Delta t/2$. The third term in Eq. (32) is responsible for keeping red and blue separated across the interface zone by creating an effective antidiffusion. The second term is included to avoid an undesirable force dependence arising in the continuum limit of this model. The details of the continuum dynamics obtained in the long-wavelength limit using this algorithm are given in Appendix D. In Appendix E we have used the results found for this continuum limit of region II to give an analytical estimate for the width of the fluid-fluid interface zone.

Through normal diffusion being opposed by antidiffusion, the above algorithm achieves phase separation in a way analogous to that of the Cahn-Hilliard approach [10,11]. However, because we use the window function of Eq. (33) to gradually turn off the antidiffusion at the limits of the finite-width transition layer, we do not need to incorporate a Laplacian of the color field into the effective chemical potential as is required to obtain stable results in the Cahn-Hilliard approach.

The goal for the modeling of blue concentration in region II is that blue particles can advance from high to low concentrations while maintaining the color separation once equilibrium is attained. Throughout this process, surface tension needs to be allowed to develop with interface curvature. The above model, with the competing diffusive and antidiffusive fluxes and the volumetric interfacial force, accomplishes all of these requirements.

IV. NUMERICAL SIMULATIONS

We now implement the above scheme numerically using a D2Q9 lattice. Lattice velocities and the corresponding lattice weights are presented in Table I. In this model $c_S^2=1/3$.

In a first example, an interface moves due to diffusion alone (no flow). An analytical solution is available in this case to compare to the numerical results. In a second example, a

TABLE I. Lattice weights and velocities for the D2Q9 lattice.

Lattice direction	$\mathbf{c}_\alpha(\Delta x/\Delta t)$	w_α
$\alpha = 0$	(0,0)	4/9
$\alpha = 1,\ldots,4$	$(\pm1,0),(0,\pm1)$	1/9
$\alpha = 5,\ldots,8$	$(\pm1,\pm1),(\mp1,\pm1)$	1/36

bubble of one fluid is allowed to dissolve into the other, up to the solubility limit. In the final examples, we consider how flow and diffusion compete in controlling the concentrations in front of an interface moving due to flow.

In the simulations, we have set the initial particle mass density ρ, lattice constant Δx, and time step Δt equal to unity. For simplicity, the kinematic viscosity of both fluids are set to $\nu = 0.1$ in all our simulations. In addition, we have set the color gradient threshold $\bar{n} = 2 \times 10^{-3}$.

A. One-dimensional diffusion problem with a freely moving interface

A feature of the LB model developed in this paper is that it allows one phase to diffuse into the other, which results in a movement of the interface position even in the absence of flow. There are few exact analytical results that involve a freely moving interface, because specifying boundary conditions on an interface, whose position must also be determined as part of the problem, makes the problem nonlinear. Fortunately, a simple one-dimensional case does have exact analytical solutions.

Consider an infinite plane interface between the red and blue fluids with a normal in the x direction. Initially, at $t = 0$, the interface separating pure blue ($x > 0$) from pure red ($x < 0$) is at $x = 0$. Blue is then allowed to diffuse into red (while red is not allowed to enter blue), which causes the interface position $x = s(t)$ to advance in the $+x$ direction starting from its initial position of $s(0) = 0$. The plane $x = 0$ is maintained as pure red for all time. We need to determine how the concentration $\varphi(x,t)$ of blue in red is evolving in the binary-fluid region $0 < x < s(t)$ and determine $s(t)$.

The concentration $\varphi(x,t)$ in this case satisfies the diffusion equation $\partial\varphi/\partial t = D_0\partial^2\varphi/\partial x^2$ and is subject to the two boundary conditions $\varphi(x = s(t),t) = \alpha_2$ and $\varphi(x = 0,t) = 0$. The condition that allows the unknown interface position $s(t)$ to be determined is that the diffusive flux of blue particles out of the interface $j_x = -\rho_- D_0\partial\varphi/\partial x|_{x=s(t)}$ is balanced by the interface movement $\rho_{\mathrm{B}+}ds(t)/dt$. Here the interface is taken as a step with ρ_- the total mass density on the s_- side of the interface and $\rho_{\mathrm{B}+}$ the blue mass density on the s_+ side of the interface. In this zero-Mach-number problem, density is constant, so $\rho_- = \rho_{\mathrm{B}+} = \rho$ and $\rho_{\mathrm{B}-} = \alpha_2\rho$. The interface movement equation is then

$$\frac{ds}{dt} = D_0\left.\frac{\partial\varphi}{\partial x}\right|_{x=s(t)} \tag{34}$$

and is subject to the initial condition that $s(0) = 0$.

The above is known as a Stefan problem [33] and has a general solution $\varphi(x,t) = A + B\,\mathrm{erf}(x/\sqrt{4D_0t})$, where A and B are constants and $\mathrm{erf}u = (2/\sqrt{\pi})\int_0^u e^{-w^2}dw$ is the error function. Clearly, $A = 0$ from $\varphi(x = 0,t) = 0$. In addition, to satisfy the boundary condition on $x = s(t)$ we must have

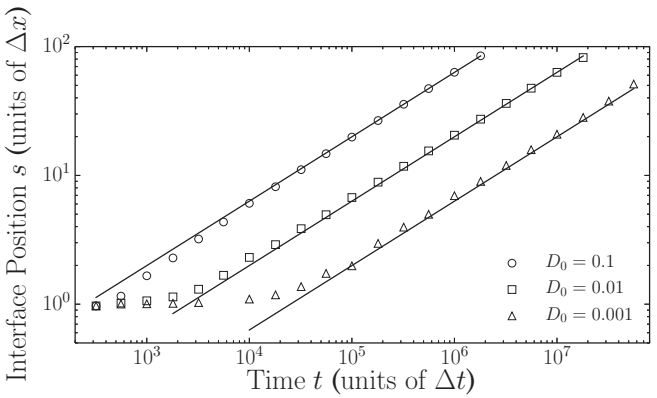

FIG. 2. Interface position s, where $\varphi = \alpha_2 = 0.02$, as a function of time t. The position and time are measured, respectively, in terms of the lattice constant Δx and the time discretization Δt. Open symbols show the numerical results, while black lines represent the analytical solutions. We have used linear interpolation to estimate subgrid positions of the interface.

both $s(t) = \zeta\sqrt{4D_0t}$, where ζ is an unknown constant, and $B = \alpha_2/\mathrm{erf}\zeta$. The constant ζ is determined from the interface movement of Eq. (34),

$$\frac{ds}{dt} = \frac{2\zeta D_0}{\sqrt{4D_0t}} = \alpha_2\frac{2D_0}{\sqrt{4\pi D_0t}}\frac{\exp(-\zeta^2)}{\mathrm{erf}\zeta}. \tag{35}$$

Altogether, we have the exact solutions

$$\varphi(x,t) = \alpha_2\frac{\mathrm{erf}\left(x/\sqrt{4D_0t}\right)}{\mathrm{erf}\zeta} \quad \text{and} \quad s(t) = \zeta\sqrt{4D_0t}, \tag{36}$$

where ζ is the positive root of

$$\frac{\alpha_2}{\sqrt{\pi}}\frac{\exp(-\zeta^2)}{\zeta\,\mathrm{erf}\zeta} - 1 = 0. \tag{37}$$

Due to the monotonic nature of Eq. (37), there is a single positive root that can be determined using any preferred numerical root finder; we find that $\zeta = 0.0997$, having chosen $\alpha_2 = 0.02$.

For the lattice Boltzmann modeling of the above, the system is initialized with $\rho(\mathbf{x},0) = 1.0$, $\mathbf{u}(\mathbf{x},0) = 0$, and $\rho_{\mathrm{B}}(\mathbf{x},0) = \rho(\mathbf{x},0)$. In addition, we have the boundary conditions $\rho_{\mathrm{B}}(0,t) = 0$ and $\rho_{\mathrm{B}}(L_x,t) = \rho(L_x,0)$, where $L_x = 100$ is the system length [the interface position lies within $0 < s(t) < L_x$]. We have included a periodic y direction, which makes the simulations one dimensional in nature. We have set the interfacial tension to be $\sigma = 10^{-4}$ in lattice units, but since the interface will remain flat throughout the simulations this does not have any influence on the results. We have used $\beta = 1$ in the recoloration step of Eq. (32) to ensure a thin interface region. In the initial stages of the simulations, the equilibration of the emergent interface between the two fluid phases will result in some deviations from the position predicted from the analytical results. This is a transient effect that is not part of the diffusive process being treated. To minimize this initial deviation we choose in this comparison a conservative solubility of $\alpha_2 = 0.02$. In the simulations we identify the position $x = s(t)$ of the interface as being where $\varphi = \alpha_2$. Figure 2 shows this position as a function of time for three different diffusivities. We see that there are some

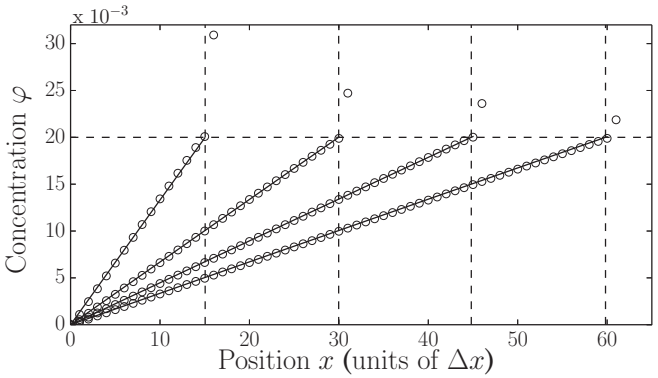

FIG. 3. Concentration profiles for $D_0 = 0.1$ and $\alpha_2 = 0.02$ as a function of position. Open circles represent the numerical results. Solid black lines show the analytical solution. Vertical dashed lines indicate, from the left, the position of the fluid interface at times $t = [57.0 \times 10^3, 226 \times 10^3, 505 \times 10^3, 900 \times 10^3]$, respectively. The horizontal dashed line marks the saturation concentration α_2.

deviations in the positions initially but that the agreement is generally good. In Fig. 3, the concentration profiles to the left of the moving interface at four different times are displayed. The profiles retrieved from the simulations are observed to be close to those given by the analytical solution.

B. Bubble evaporation

To demonstrate how our algorithm equilibrates at the desired solubility levels in a closed system, we consider an evaporating bubble located in the center of a circularly confined system. The diameter of this system is in the simulations set to 100 lattice units. Initially, the bubble consists of pure blue fluid ($\varphi = 1.0$) and the surrounding phase is pure red fluid ($\varphi = 0$). The bubble will evaporate until the

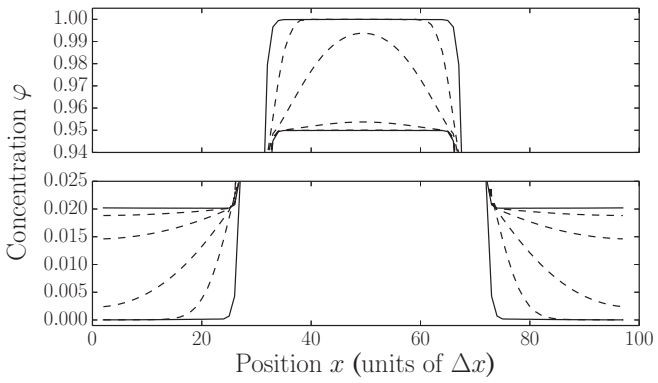

FIG. 4. Concentration profiles of a blue fluid bubble at different times during evaporation. The concentrations φ are given as functions of position measured in terms of the lattice constant Δx. In this simulation the solubility levels are given by $\alpha_1 = 0.95$ and $\alpha_2 = 0.02$. The bubble radius was here initiated to be $r_0 = 20$ lattice units. The concentration profiles are plotted at time steps $t' = t - t_0 = [0.0, 1.0 \times 10^3, 1.0 \times 10^4, 5.0 \times 10^4, 1.0 \times 10^5, 5.0 \times 10^5]$, where $t_0 = 10^4$ was the initiation time for the evaporation process. To better see the behavior of the diffusion process taking place, two separate regions of the concentration profiles have been cut out and magnified. The initial and final concentration profiles are shown in solid lines.

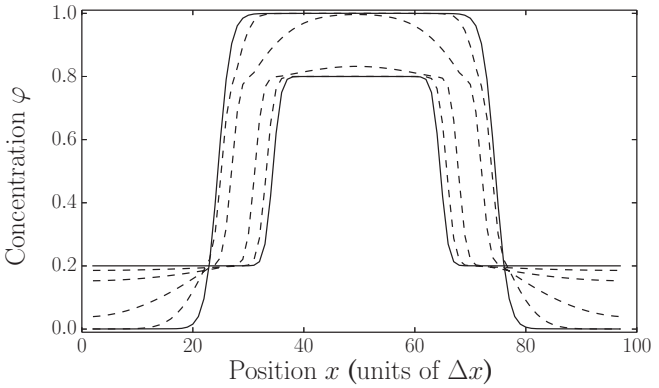

FIG. 5. Concentration profiles of an evaporating blue fluid bubble at different times as functions of position. Here $\alpha_1 = 0.8$, $\alpha_2 = 0.2$, and the initial bubble radius $r_0 = 25$ lattice units. The concentration profiles are plotted for the same time steps as in Fig. 4. The initial and final concentration profiles are as in Fig. 4 represented by solid lines.

concentration levels in the two phases equal the solubility levels given by α_1 and α_2. In the simulations, the interface is initially allowed to equilibrate for a time t_0 before the evaporation process is started.

Figures 4 and 5 show the concentration profiles for two evaporation processes where the solubility levels differ considerably. For the sake of comparison, both simulations use the diffusivities $D_B = 0.01$ and $D_R = 0.0025$ and the interfacial tension is set to $\sigma = 10^{-4}$ (all in lattice units). Figure 4 shows a dissolution process where the solubility levels are set to $\alpha_1 = 0.95$ and $\alpha_2 = 0.02$. This system exhibits solubility levels similar to those of pure water (blue) in a cell of pure supercritical CO_2 (red) at a temperature of 313 K and a pressure of 7 MPa. Figures 5 and 6 present a system with considerably larger solubility levels. Here $\alpha_1 = 0.8$ and $\alpha_2 = 0.2$. Because of these large solubility levels, a radical decrease in the bubble radius is observed. From Fig. 6 we see that the pressure

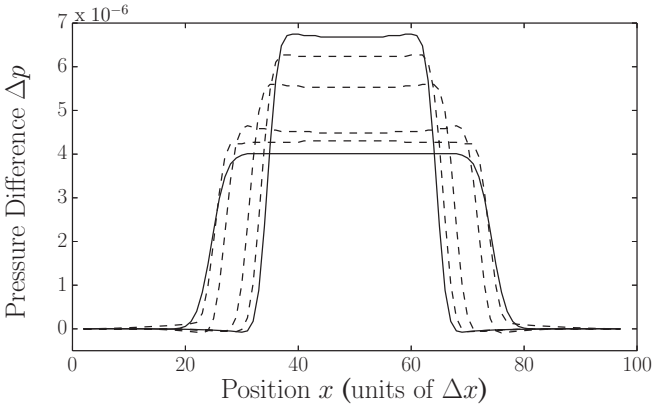

FIG. 6. Pressure profiles of an evaporating bubble as functions of position. This figure shows the same system as Fig. 5 and the profiles plotted are at the same time steps as in Figs. 4 and 5. The pressure difference Δp is the difference between the measured pressure at position x and the pressure measured at a point outside the bubble, far away from the interface region between the two phases. The pressure is given in lattice units.

increases as expected as the bubble radius decreases during evaporation. With these large solubility levels, the transition from diffusion inside region II to outside region I can be abrupt, leading to noisy results, if the transition width is too small. To smooth out the transition, we used a value of $\beta = 0.5$ to produce the results presented in Figs. 5 and 6, as opposed to $\beta = 0.8$ in Fig. 4.

C. Péclet-number-dependent invasion processes

The main motivation for developing this algorithm was to gain the ability to simulate partial dissolution of fluids during transport in porous media. We will here look at some examples of such processes.

We start off with studying dissolution of a single meniscus advancing due to flow in a straight channel, before presenting a similar process occurring in a two-dimensional porous medium with a number of menisci present. Let us define our coordinate system so that the x axis is parallel to the flow direction, while the y axis is in the perpendicular direction. In the y direction, the system is confined by solid walls. These are simulated by using a simple bounceback rule that replaces the regular interaction equations at the wall sites [13]. The wetting property of the walls is modeled by modifying the color gradient $\mathbf{n}$ at sites next to wall sites [34]. Here the neighboring color difference $\tilde{c}(\mathbf{x} + \mathbf{c}_\alpha \Delta t, t)$ at wall sites is given by $\tilde{c}_{\text{wall}} = -\cos\theta_w$, where θ_w is the static contact angle. If $\theta_w = 0$, the invading fluid is perfectly nonwetting. If $\theta_w = 180$, the invading fluid perfectly wets the solid surface. However, if the fluid diffusing into the other phase is not perfectly nonwetting, care must be taken. Beyond a certain value for the wetting angle, the equilibrium concentration of the diffusing phase next to a wall site can attain values between α_1 and α_2. This means that sites next to a wall can have an absolute value of the color gradient $|\mathbf{n}| > \bar{n}$ in a region away from the intended interface region. This has the effect of distorting the spatial shape of region II and subsequently giving unphysical behavior in regions close to wall sites. By treating sites next to wall sites separately from the other fluid sites and introducing a modified concentration criterion for those sites, preliminary results show that this distortion of region II can be eliminated. In this paper we will not explore this behavior and will simply limit our examples to a perfectly nonwetting diffusing fluid phase.

Injection of an invading fluid into a system, initially filled with a defending fluid, is modeled by letting the system boundaries perpendicular to the flow be periodic to the total fluid distribution f_i, but with the additional requirement that all incoming populations on the injection side are blue while all incoming populations at the opposite boundary are red. At the recoloration boundaries, the local color gradient is set to zero to avoid any phase separation and surface tension effects.

The injection of fluid is driven at a constant rate. This invasion rate is maintained by a uniform volume force $F_x(t)$ acting in the x direction [35]. Using a global flux-controlling volume force rather than applying a constant flux boundary condition minimizes the effects of the inherent compressibility in our LB algorithm. The volume force $F_x(t)$ varies in time as

$$\frac{\partial F_x(t)}{\partial t} = K_P[J_0 - J_x(t)] - K_D \frac{\partial J_x(t)}{\partial t}. \tag{38}$$

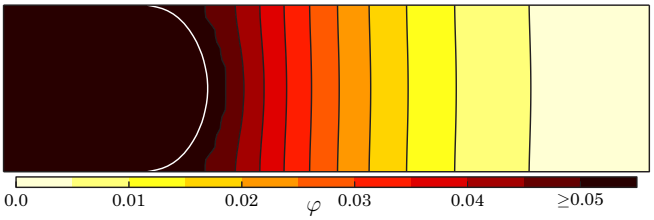

FIG. 7. (Color online) Snapshot of an invading fluid being injected from the left side of a straight channel, while it partially dissolves in a defending fluid. The figure shows the invading fluid concentration at $t = 7.5 \times 10^4$ with $\text{Pe} = 3 \times 10^{-1}$ and $\text{Ca} = 10^{-2}$ ($J_x = 10^{-4}$, $\sigma = 10^{-3}$, and $D_0 = 10^{-2}$). The color scale (grayscale) is a linear scale showing the invading fluid concentration φ. The thin white line represents the interface between the two fluids.

Here J_0 is the desired mass flux density in the x direction and $J_x(t)$ is the mean mass flux density measured in the system at time t. The positive tuning parameters K_P and K_D determine the response of the body force. In the simulation, these are set to $K_p = 1.0$ and $K_D = 0.4$. In the simulations we set the interface thickness parameter to $\beta = 1.0$, the solubility levels to $\alpha_1 = 1.0$ and $\alpha_2 = 0.05$, and the contact angle to $\theta_w = 0$.

The behavior for this type of system is controlled by the values of the two key dimensionless numbers: the Péclet number Pe and the capillary number Ca. The capillary number may be defined as the ratio of viscous shear stress to capillary pressure and is given by

$$\text{Ca} = \frac{J_x \nu}{\sigma}, \tag{39}$$

where J_x is the mass flux density (J_x/ρ is the average fluid velocity). The Péclet number is the ratio of flow speed to diffusion speed and is given by

$$\text{Pe} = \frac{J_x l}{\rho D_0}, \tag{40}$$

where l is the characteristic length over which diffusion occurs, which we take to be the channel width in the set of channel flow simulations and the average pore throat width in the porous medium simulations.

We next turn to dissolution across a single meniscus advancing due to flow in a straight channel with a length $L_x = 120$ and a height $L_y = 30$ measured in lattice units. In Figs. 7–9, the flow begins at $t = 0$ with the fluid interface at position $x = 20$. When $\text{Pe} < 1$, the diffusion advances more rapidly than the meniscus and the concentration in front of the meniscus will behave as shown in Fig. 7. When $\text{Pe} > 1$, the diffusion front remains closer to the meniscus as in Fig. 8.

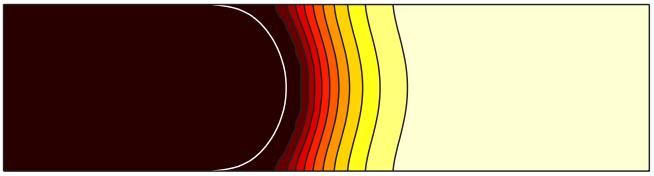

FIG. 8. (Color online) Snapshot of the invading fluid concentration φ at $t = 1.5 \times 10^5$ with $\text{Pe} = 3$ and $\text{Ca} = 10^{-2}$ ($J_x = 10^{-4}$, $\sigma = 10^{-3}$, and $D_0 = 10^{-3}$). See Fig. 7 for further description.

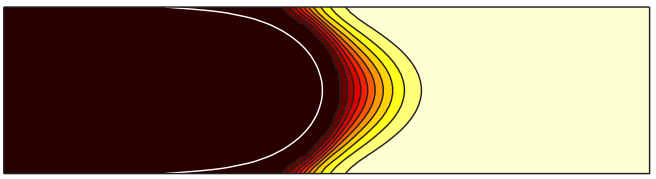

FIG. 9. (Color online) Snapshot of the invading fluid concentration φ at $t = 3.0 \times 10^4$ with Pe = 30 and Ca = 10^{-1} ($J_x = 10^{-3}$, $\sigma = 10^{-3}$, and $D_0 = 10^{-3}$). The capillary number was increased by increasing the rate of injection. See Fig. 7 for further description.

In both of these examples, the capillary number Ca is small enough that capillary forces maintain the shape of the meniscus even as it moves down the channel at the rate of injection. The Péclet number Pe was changed here by changing the diffusivity. Finally, in Fig. 9, Ca is increased by increasing the injection rate with the result that the shape of the meniscus is now altered by viscous shearing. The viscous shear forces are able during the invasion to distort the form of the meniscus from its equilibrium shape, causing it to continuously stretch in the flow direction. The greater flow velocity down the center of the channel also results in the enhanced advection of concentration observed. A finger of advected concentration advancement begins to develop in the center of the channel due to the enhanced fluid velocity there. All of this is as qualitatively expected.

Finally, we perform invasion simulations for a two-dimensional inert porous medium. Here the medium is made up of approximately 30×15 randomly distributed circular disks (see Fig. 10) on a lattice of 400×200 grid points. The invading fluid is injected into the porous medium initially filled with a defending fluid. While being injected, the invading fluid is allowed to mix with the defending fluid up to a solubility limit of $\alpha_2 = 0.05$. The wetting properties of the porous medium are again modeled by the bounceback rule described earlier with a contact angle of $\theta_w = 0$. We perform two simulations with a fixed injection rate and interface tension, maintaining the same capillary number Ca = 10^{-2} for both simulations. The only difference between the two are the diffusivity of the invading phase in the defending one. Figure 10 shows a comparison of the initial invasion process in the two simulations. The left column of the figure shows the time evolution of a process where Pe = 7×10^{-1}, while in the right column the Pe = 7×10^{-2}. The most obvious difference between the two simulations is the width of the diffusion front. Since the solubility limit α_2 of the invading phase in the defending one is relatively low, there are limited changes in the invasion structure due to the differences in diffusivity. However, it is possible to see signs of the higher rate of dissolution, as is expected, in the invasion structure of the process having a lower Péclet number. This is easiest to see when comparing the two bottom panels of Fig. 10. Since the invading fluid is being injected into the porous material at the same constant rate in the two simulations, there should at a given time be the same amount of invading fluid in both systems so long as no injected fluid has reached the outlet. Due to the higher dissolution rate in the process depicted in the right column in Fig. 10, the average position of the invasion front at a given time is observed to lag slightly behind that of the process shown in the left column.

V. CONCLUSION

A lattice Boltzmann method has been introduced that allows for diffusive mixing between the two fluids during two-phase flow. Numerical examples of bubble evaporation and how concentration profiles in flowing fluids depend on Péclet number and capillary number were presented. The algorithm is directly applicable to problems such as how flowing bubbles dissolve their contents into the surrounding fluid and how one fluid invades another in porous media.

The essence of the algorithm is to define two regions in the fluid system: (i) a finite-width interfacial region separating the fluids in which both color separation and surface tension are allowed for and (ii) all other regions in which the binary fluids behave as being perfectly miscible with concentrations governed by the advection-diffusion equation. The location of the interfacial region is defined by giving the concentration level of one of the fluids at the boundary as fixed inputs. These concentration levels at the boundary between the two regions define the equilibrium solubility level in each fluid. It was not found necessary to perform special interpolation between node points to define the precise position of the concentration surfaces at the limits of the interfacial region. However, it was observed that as the solubility levels increased to above around 10%, the transition of diffusion from the interfacial zone to the miscible zone could be too abrupt if the transition zone was too narrow. The result was anomalous (noisy) concentration values near the edge of the interfacial region. This numerical artifact was avoided by simply decreasing the parameter β in the recoloration step, which has the effect of widening, and therefore smoothing, the transition between the regions.

In the paper the algorithm was used to simulate a simple analytically solvable problem, before applying it to situations of bubble evaporation and situations of invasion processes where dissolution occurs. Future research involving this algorithm could be to allow for the surface tension and possibly contact angle to change as the fluids diffusively equilibrate.

ACKNOWLEDGMENTS

The work of O.A. was supported as part of the Center for Nanoscale Control of Geologic CO2, an Energy Frontier Research Center funded by the US Department of Energy, Office of Science, Office of Basic Energy Sciences under Grant No. DE-AC02-05CH11231. The work of S.R.P. was performed under the auspices of the US Department of Energy, at the Lawrence Berkeley National Laboratory, under Contract No. DE-AC02-05CH11231. Support was provided specifically by the Geosciences Research Program of the DOE Office of Basic Energy Sciences, Divisions of Chemical Sciences, Geosciences and Biosciences.

APPENDIX A: CHAPMAN-ENSKOG EXPANSION OF THE LATTICE BOLTZMANN EQUATION

Having an LBE

$$j_\alpha(\mathbf{x} + \mathbf{c}_\alpha \ \Delta t, t + \Delta t) - j_\alpha(\mathbf{x},t) = \lambda[j_\alpha(\mathbf{x},t) - j_\alpha^{\mathrm{eq}}(\mathbf{x},t)] + \Delta j_\alpha^F(\mathbf{x},t), \quad \text{(A1)}$$

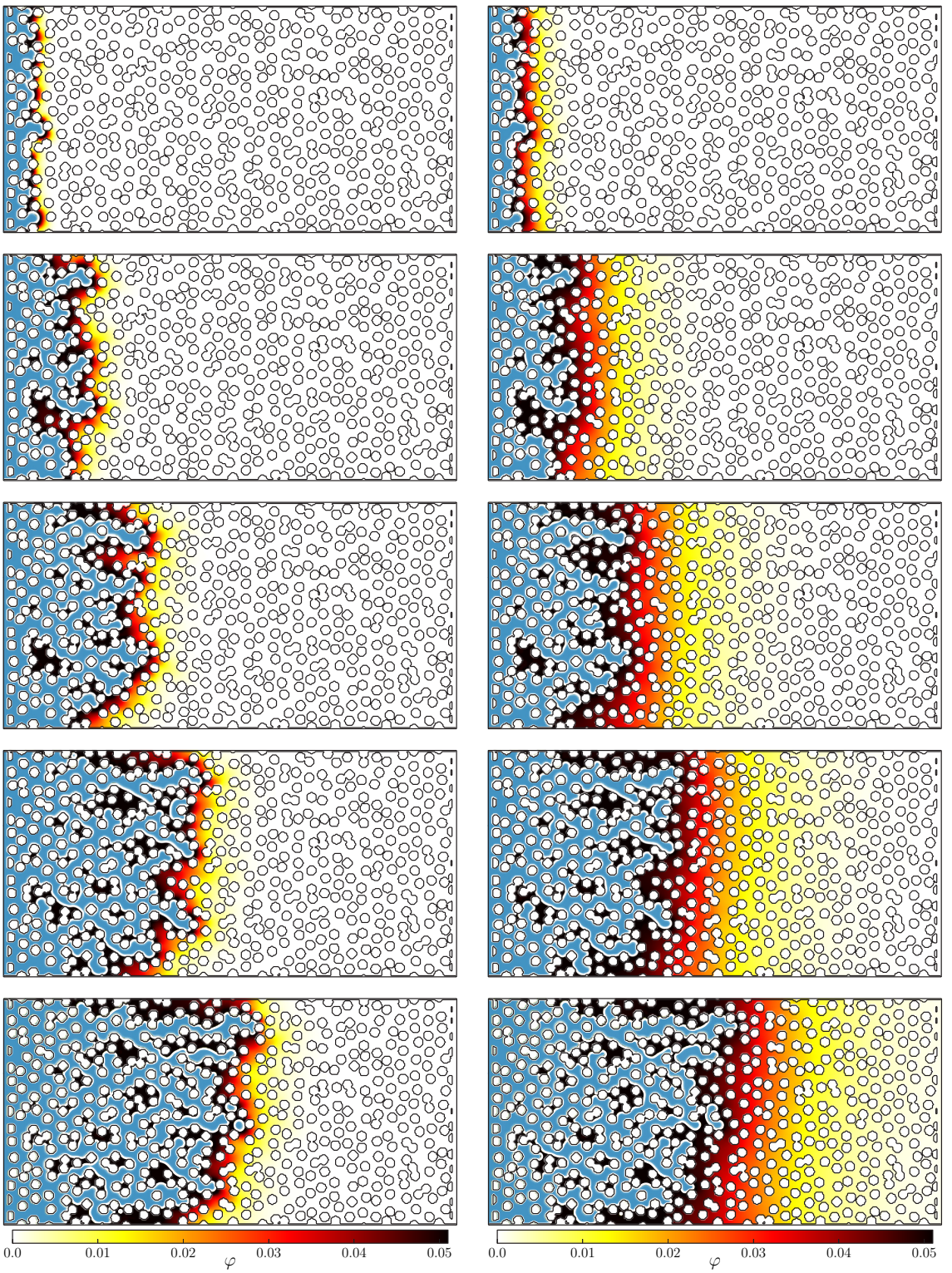

FIG. 10. (Color online) For a capillary number $\mathrm{Ca} = 10^{-2}$, two invasion processes, where partial fluid dissolution occurs, are compared at different times. In both processes, an invading fluid is, while being injected from the left side of a porous medium, dissolving into the defending fluid. The porous structure is shown as white areas outlined in black. Each column shows one experiment where the images are ordered, from the top, by increasing time. The two pictures in each row depict the same instants in time. The invasion structure, i.e., the pure invading fluid, is presented in blue (dark gray), extending from the left side of the system. The invading fluid dissolved in the defending one is represented by a linear color scale (grayscale) given below the last image in each column. The darkest shade represents $0.5 \geqslant \varphi \geqslant \alpha_2 = 0.05$, while the lightest shade represents $\varphi = 0$. The left column shows the structure evolution of an invasion process characterized by $\mathrm{Pe} = 7 \times 10^{-1}$ ($J_x = 10^{-3}$, $\nu = 10^{-1}$, $\sigma = 10^{-2}$, and $D_0 = 10^{-2}$). In the right column, a similar process with $\mathrm{Pe} = 7 \times 10^{-2}$ ($J_x = 10^{-3}$, $\nu = 10^{-1}$, $\sigma = 10^{-2}$, and $D_0 = 10^{-1}$) is presented.

where $j_\alpha \in \{f_\alpha, g_\alpha\}$ and $\lambda \in \{\lambda_\nu, \lambda_D\}$, performing a Chapman-Enskog expansion will retrieve the desired continuum dynamics equations presented in Eqs. (1)–(4). This may be done by introducing an expansion parameter ε such that

$$j_\alpha = \sum_{n=0}^{\infty} \varepsilon^n j_\alpha^{(n)}, \tag{A2}$$

$$\partial_t = \sum_{n=1}^{\infty} \varepsilon^n \partial_{tn} \quad \text{and} \quad \partial_i = \sum_{n=1}^{\infty} \varepsilon^n \partial_{in}. \tag{A3}$$

The parameter ε is often taken to be proportional to the Knudsen number, which is here the ratio of the lattice spacing to a characteristic macroscopic length scale.

The Taylor series

$$j_\alpha(\mathbf{x} + \mathbf{c}_\alpha \Delta t, t + \Delta t) = \sum_{m=0}^{\infty} \frac{(\Delta t)^m}{m!} D_\alpha^m j_\alpha(\mathbf{x}, t) \tag{A4}$$

gives, through second order in Δt, the following hierarchy of LBEs at increasing orders of ε:

$$O(\varepsilon^0): \; j_\alpha^{(0)} = j_\alpha^{\mathrm{eq}}, \tag{A5}$$

$$O(\varepsilon^1): \; \Delta t D_{\alpha 1} j_\alpha^{(0)} = \lambda j_\alpha^{(1)} + \Delta j_\alpha^{F(1)}, \tag{A6}$$

$$O(\varepsilon^2): \; \partial_{t2} j_\alpha^{(0)} = \frac{\lambda}{\Delta t} j_\alpha^{(2)} - D_{\alpha 1}\left[\left(1 + \frac{\lambda}{2}\right) j_\alpha^{(1)} + \frac{1}{2} \Delta j_\alpha^{F(1)}\right], \tag{A7}$$

where we have adopted a Chapman-Enskog multiscale expansion where $\partial_t = \varepsilon \partial_{t1} + \varepsilon^2 \partial_{t2} + O(\varepsilon^3)$ and $\partial_i = \varepsilon \partial_{i1} + O(\varepsilon^2)$. In addition, we have used that $\Delta j_\alpha^F = \varepsilon \Delta j_\alpha^{F(1)}$ and defined

$$D_\alpha = \sum_{n=1}^{\infty} \varepsilon^n D_{\alpha n} \equiv \sum_{n=1}^{\infty} \varepsilon^n (\partial_{tn} + c_{\alpha i} \partial_{in}). \tag{A8}$$

This derivative should not to be confused with the macroscopic material derivative $D_t \equiv (\partial_t + u_i \partial_i)$. In the following we will also need that

$$\sum_\alpha w_\alpha = 1, \tag{A9}$$

$$\sum_\alpha w_\alpha c_{\alpha i} c_{\alpha j} = c_S^2 \delta_{ij}, \tag{A10}$$

$$\sum_\alpha w_\alpha c_{\alpha i} c_{\alpha j} c_{\alpha k} c_{\alpha l} = c_S^4 (\delta_{ij}\delta_{kl} + \delta_{ik}\delta_{jl} + \delta_{il}\delta_{jk}), \tag{A11}$$

while similar sums over an odd number of the velocity vectors $\mathbf{c}_i$ are equal to zero. We will use these equations and properties to derive the continuum dynamics equations in Appendixes B–D.

APPENDIX B: DERIVATION OF THE NAVIER-STOKES EQUATIONS

The distribution function of the combined fluids f_α obeys in both region I and region II an LBE of the form presented in Appendix A. If we now replace the generic distribution j_α with the one of the combined fluids, a direct sum of Eq. (A5) over all lattice directions combined with Eq. (10) yields

$$\sum_\alpha f_\alpha^{(0)} = \rho, \tag{B1}$$

so

$$\sum_\alpha f_\alpha^{(n)} = 0 \quad \text{for } n \geqslant 1. \tag{B2}$$

Similarly, a weighted sum of Eq. (A5) using $c_{\alpha i}$ as weights leads to

$$\sum_\alpha f_\alpha^{(0)} c_{\alpha i} = \rho u_i. \tag{B3}$$

Combined with $F_i = \varepsilon F_{i1}$ and the definition $\rho u_i = \sum_\alpha f_\alpha c_{\alpha i} + \Delta t F_i/2$, this gives us that

$$\sum_\alpha f_\alpha^{(1)} c_{\alpha i} = -\Delta t F_{i1}/2 \tag{B4}$$

and

$$\sum f_\alpha^{(n)} c_{\alpha i} = 0 \quad \text{for } n \geqslant 2. \tag{B5}$$

We will further need the two additional results

$$\sum_\alpha f_\alpha^{(0)} c_{\alpha i} c_{\alpha j} = c_S^2 \rho \delta_{ij} + \rho u_i u_j, \tag{B6}$$

$$\sum_\alpha f_\alpha^{(0)} c_{\alpha i} c_{\alpha j} c_{\alpha k} = c_S^2 \rho (\delta_{ij} u_k + \delta_{ik} u_j + \delta_{jk} u_i). \tag{B7}$$

A direct sum of Eq. (A6) over all the lattice directions, combined with Eq. (12), yields

$$\partial_{t1} \rho + \partial_{j1}(\rho u_j) = 0. \tag{B8}$$

A weighted sum of Eq. (A6) using $c_{\alpha i}$ as weight leads to

$$\partial_{t1}(\rho u_i) + \partial_{j1}\left(c_S^2 \rho \delta_{ij} + \rho u_i u_j\right) = F_{i1}, \tag{B9}$$

where we again have used Eq. (12). Identifying $p = \rho c_S^2$ as the pressure, which is consistent with c_S being the speed of sound, shows that the previous equation may be considered a form of Euler's equation where $c_S^2 \rho \delta_{ij} + \rho u_i u_j$ is identified as the component form of the inviscid momentum flux tensor $\Pi_{ij}^{(0)}$.

The direct sum of Eq. (A7) gives

$$\partial_{t2} \rho = 0, \tag{B10}$$

while the weighted sum of Eq. (A7) using $c_{\alpha i}$ as weight yields

$$\partial_{t2}(\rho u_i) = -\partial_{j1} \sum_i \left[\left(1 + \frac{\lambda_\nu}{2}\right) f_\alpha^{(1)} + \frac{1}{2} \Delta f_\alpha^{F(1)}\right] c_{\alpha i} c_{\alpha j}. \tag{B11}$$

By using Eq. (A6) to express $f_\alpha^{(1)}$, combined with Eqs. (B6) and (B7), this equation may be rewritten as

$$\partial_{t2}(\rho u_i) = -\partial_{j1}\left\{\left(\frac{1}{\lambda_\nu}+\frac{1}{2}\right)c_S^2\Delta t\left[\partial_{i1}(\rho u_j)+\partial_{j1}(\rho u_i) + \partial_{t1}\left(\frac{\rho u_i u_j}{c_S^2}\right)\right] - \frac{1}{\lambda_\nu}\sum_\alpha \Delta f_\alpha^{F(1)} c_{\alpha i}c_{\alpha j}\right\}. \tag{B12}$$

Employing again the expression for Δf_α^F from Eq. (12), combined with the continuity equation (B8) and Euler's equation (B9), we have that

$$\partial_{t2}(\rho u_i) = \partial_{j1}\left\{\rho\nu\left[\partial_{i1}u_j+\partial_{j1}u_i+\frac{\partial_{k1}(\rho u_i u_j u_k)}{\rho c_S^2}\right]\right\}, \tag{B13}$$

where we also have defined $\nu \equiv -(1/\lambda_\nu + 1/2)c_S^2\Delta t$. If we neglect the last unwanted $O(u^3)$ term we have obtained exactly the expression we have been seeking. Observe that the force term, Δf_α^F introduced by Guo *et al.*, results in no unwanted body force terms in the continuum equations. Bringing the above equations together through $O(\varepsilon^2)$, using that $\partial_t = \varepsilon\partial_{t1} + \varepsilon^2\partial_{t2} + O(\varepsilon^3)$ and $\partial_i = \varepsilon\partial_{i1} + O(\varepsilon^2)$, gives

$$\partial_t\rho + \partial_i(\rho u_i) = 0, \tag{B14}$$

$$\rho\left(\partial_t u_i + u_j\partial_j u_i\right) = -\partial_i p + F_i + \partial_j\{\rho\nu[\partial_i u_j + \partial_j u_i + O(u^3)]\} + O(\varepsilon^2), \tag{B15}$$

which are the Navier-Stokes equations we wanted to retrieve. On comparison to Eq. (2) combined with Eq. (3), we see that in this LB model the bulk viscosity would, in a d-dimensional system, be directly related to the shear viscosity as $\xi = 2\rho\nu/d$.

APPENDIX C: DERIVATION OF THE ADVECTION-DIFFUSION EQUATION

In region I, the zone away from the fluid-fluid interface, the distribution function for one of the fluid components g_α (here denoted as the blue fluid component) obeys an LBE of the form presented in Appendix A. If we replace the generic j_α with the distribution function g_α, a direct sum of Eq. (A5) over all lattice directions combined with Eq. (27) gives

$$\sum_\alpha g_\alpha^{(0)} = \rho_B \tag{C1}$$

and therefore

$$\sum_\alpha g_\alpha^{(n)} = 0 \quad \text{for } n \geqslant 1. \tag{C2}$$

Further, one also has

$$\sum_\alpha g_\alpha^{(0)} c_{\alpha i} = \rho_B u_i. \tag{C3}$$

A direct sum of Eq. (A6) for g_α over the lattice directions α, combined with Eq. (26), yields

$$\partial_{t1}\rho_B + \partial_{j1}(\rho_B u_j) = 0, \tag{C4}$$

while a direct sum of Eq. (A7) for g_α gives

$$\partial_{t2}\rho_B = -\sum_\alpha D_{\alpha 1}\left[\left(\frac{1}{\lambda_D}+\frac{1}{2}\right)\left(\Delta t D_{\alpha 1} g_\alpha^{(0)} - \Delta g_\alpha^{F(1)}\right)\right] - \frac{1}{2}\sum_\alpha D_{\alpha 1}\Delta g_\alpha^{F(1)}. \tag{C5}$$

Through inserting the expression for $g_\alpha^{(0)} = g_\alpha^{\rm eq}$ from Eq. (27) and using Eqs. (26), (C4), (B8), and (B9) and that $\rho_B = \varphi\rho$, we obtain after some algebra

$$\begin{aligned}\partial_{t2}\rho_B &= -\partial_{i1}\left[\left(\frac{1}{\lambda_D}+\frac{1}{2}\right)c_S^2\Delta t\rho\partial_{i1}\varphi + \left(\frac{1}{\lambda_D}+\frac{1}{2}\right)\varphi\Delta t F_{i1} - \frac{1}{\lambda_D}\sum_\alpha \Delta g_\alpha^{F(1)} c_{\alpha i}\right] \\ &= -\partial_{i1}\left[\left(\frac{1}{\lambda_D}+\frac{1}{2}\right)c_S^2\Delta t\rho\partial_{i1}\varphi\right].\end{aligned} \tag{C6}$$

Bringing it together through $O(\varepsilon^2)$, using that $\partial_t = \varepsilon\partial_{t1} + \varepsilon^2\partial_{t2}$ and $\partial_i = \varepsilon\partial_{i1}$, gives

$$\partial_t\rho_B + \partial_i(\rho_B u_i) = \partial_i(D_0\rho\partial_i\varphi), \tag{C7}$$

where D_0 is the diffusion coefficient of blue particles given by

$$D_0 = -\left(\frac{1}{\lambda_D}+\frac{1}{2}\right)c_S^2\Delta t. \tag{C8}$$

By using the conservation of mass given by Eq. (B14) and the definition $\rho_B = \varphi\rho$, some final rearrangement gives the advection-diffusion equation in exactly the desired form

$$\rho(\partial_t\varphi + u_i\partial_i\varphi) = \partial_i(D_0\rho\partial_i\varphi). \tag{C9}$$

This result through $O(\varepsilon^2)$ has no extra unwanted error terms to this order.

APPENDIX D: CONTINUUM LIMIT OF THE PHASE SEPARATION DYNAMICS AT THE FLUID-FLUID INTERFACE (REGION II)

In the phase separation zone of region II we have, for the blue fluid distribution, that

$$g_\alpha(\mathbf{x}+\mathbf{c}_\alpha\Delta t, t+\Delta t) = \varphi f_\alpha(\mathbf{x},t) + \frac{\varphi\Delta t}{2c_S^2}w_\alpha c_{\alpha j}F_j + \beta h_\varphi\rho w_\alpha\frac{c_{\alpha i}n_i}{|\mathbf{c}_\alpha||\mathbf{n}|}, \tag{D1}$$

where n_i are the vector components of the color gradient $\mathbf{n}$. Using the expansions of Eqs. (A2)–(A4), through second order in Δt, the following hierarchy of equations at increasing orders of ε emerge:

$$O(\varepsilon^0):\ g_\alpha^{(0)} = \varphi f_\alpha^{(0)} + \beta h_\varphi\rho w_\alpha\frac{c_{\alpha i}n_i}{|\mathbf{c}_\alpha||\mathbf{n}|}, \tag{D2}$$

$$O(\varepsilon^1):\ g_\alpha^{(1)} + \Delta t D_{\alpha 1} g_\alpha^{(0)} = \varphi f_\alpha^{(1)} + \frac{\varphi\Delta t}{2c_S^2}w_\alpha c_{\alpha j}F_{j1}, \tag{D3}$$

$$O(\varepsilon^2):\ g_\alpha^{(2)} + \Delta t\partial_{t2}g_\alpha^{(0)} = -\Delta t D_{\alpha 1} g_\alpha^{(1)} + \frac{1}{2}(\Delta t)^2 D_{\alpha 1}^2 g_\alpha^{(0)} + \varphi f_\alpha^{(2)}. \tag{D4}$$

In the following we will, in addition to Eqs. (A9) and (A10), need that

$$\sum_\alpha w_\alpha \frac{c_{\alpha i} c_{\alpha j}}{|\mathbf{c}_\alpha|} = c_S \gamma \delta_{ij}. \tag{D5}$$

The equivalent sums over odd numbers of $\mathbf{c}_\alpha$ are zero (even if normalized by $|\mathbf{c}_\alpha|$). The parameter γ is particular to the D2Q9 model and comes out as

$$\gamma = \frac{\sqrt{3}(4+\sqrt{2})}{18} = 0.520\,982\,9. \tag{D6}$$

A direct sum of Eq. (D2) over all lattice directions, combined with Eqs. (B1) and (B2), establishes that

$$\sum_\alpha g_\alpha^{(0)} = \varphi\rho \tag{D7}$$

and

$$\sum_\alpha g_\alpha^{(n)} = 0 \quad \text{for } n \geqslant 1. \tag{D8}$$

Weighted sums of Eq. (D2), using $c_{\alpha i}$ and $c_{\alpha i} c_{\alpha j}$ as weights, lead to

$$\sum_\alpha g_\alpha^{(0)} c_{\alpha i} = \varphi\rho u_i + \beta\rho c_S \gamma h_\varphi \frac{n_i}{|\mathbf{n}|} \tag{D9}$$

and

$$\sum_\alpha g_\alpha^{(0)} c_{\alpha i} c_{\alpha j} = \varphi\rho c_S^2 \delta_{ij} + \varphi\rho u_i u_j, \tag{D10}$$

respectively. Higher-order moments will not be required to obtain results through $O(\varepsilon^2)$.

With the above established, the hierarchy of equations can be summed to produce the corresponding continuum laws. A direct sum over all lattice directions of Eq. (D3) yields

$$\partial_{t1}(\varphi\rho) + \partial_{i1}(\varphi\rho u_i) = -\partial_{i1}\left(\beta c_S \gamma \varphi\rho h_\varphi \frac{n_i}{|\mathbf{n}|}\right). \tag{D11}$$

Here $\beta c_S \gamma \rho h_\varphi n_i/|\mathbf{n}|$ corresponds to the vector components of an antidiffusive flux of blue particles from low blue concentrations to high blue concentrations. The amplitude of this antidiffusive flux is set by the control parameter β. The window function h_φ maintains the limits of region II at the set blue concentrations of α_1 and α_2. Its shape is also key to producing the antidiffusion. Once the differential operator of Eq. (D11) is distributed on the right-hand side, a term $-\beta c_S \gamma \rho |\nabla\varphi|(\partial h_\varphi/\partial\varphi)$ acts to increase blue on the high-blue-concentration side of region II and reduces blue on the low-concentration side because $\partial h_\varphi/\partial\varphi$ is negative on the high-blue-concentration side and positive on the low-concentration side. We also obtain another term $\beta c_S \gamma \rho h_\varphi \kappa$, where κ^{-1} is the radius of curvature given by Eq. (30). In cases where the radius of curvature becomes infinite (a flat interfacial region), this term is zero. For finite curvature, whether this term is increasing or decreasing, blue concentration will depend on the sign of the curvature (e.g., whether the blue fluid is wetting or nonwetting.). In addition, a third term $-\beta c_S \gamma h_\varphi (n_i/|\mathbf{n}|)\partial_i\rho$ is obtained. This term is negative everywhere in region II.

A direct sum of Eq. (D4), using Eq. (D8), gives

$$\begin{aligned}\partial_{t2}(\varphi\rho) &= -\partial_{i1}\sum_\alpha c_{\alpha i} g_\alpha^{(1)} \\ &\quad - \frac{1}{2}\Delta t \sum_\alpha (\partial_{t1} + c_{\alpha i}\partial_{i1})^2 g_\alpha^{(0)} \qquad \text{(D12)} \\ &= \Delta t \partial_{i1}\left(\frac{\rho c_S^2}{2}\partial_{i1}\varphi\right) \\ &\quad - \Delta t(\partial_{i1}u_i - \partial_{t1} + u_i\partial_{i1})\partial_{j1}\left(\beta c_S \gamma h_\varphi \rho \frac{n_j}{|\mathbf{n}|}\right). \qquad \text{(D13)}\end{aligned}$$

Going from Eq. (D12) to Eq. (D13) requires using nearly all the above results as well as the continuity equation (B8) and Euler's equation (B9).

Bringing it all together with $\partial_t = \varepsilon\partial_{t1} + \varepsilon^2\partial_{t2}$ and $\partial_i = \varepsilon\partial_{i1}$ and using mass conservation $\partial_t\rho + \partial_i(\rho u_i) = 0$ gives

$$\begin{aligned}\rho(\partial_t\varphi + u_i\partial_i\varphi) &= \frac{\Delta t c_S^2}{2}\partial_i\left(\rho\partial_i\varphi - \frac{2\beta\gamma\rho h_\varphi n_i}{c_S\Delta t|\mathbf{n}|}\right) \\ &\quad - \Delta t(\partial_i u_i - \partial_t + u_i\partial_i)\partial_j\left(\beta c_S\gamma h_\varphi\rho\frac{n_j}{|\mathbf{n}|}\right).\end{aligned} \tag{D14}$$

This is the final continuum statement, made without approximation other than the $O(\varepsilon^3)$ truncation errors, for how blue fluid particles are conserved in the LB model of region II. The key physics is contained in the balance of the fluxes inside the divergence of the first term on the right-hand side. The spatial distribution of φ across region II adjusts itself so that either blue is fluxing from high to low concentrations or the diffusion and antidiffusion are in exact balance in a manner that maintains the color separation across the transition zone.

APPENDIX E: WIDTH OF THE FLUID-FLUID INTERFACE (REGION II)

We may, from an analytical argument, estimate the width of region II in a stationary state where there is no net flux from region II into region I. From Eq. (D14) we observe that at the limits of region II where $h_\varphi \to 0$, the antidiffusive flux vanishes so that $|\nabla\varphi| \to 0$, as the limits are approached. The effect is that φ only asymptotically approaches the limit values of α_1 and α_2 and, in this sense, the width of region II would become infinite in the continuum limit if we had not introduced the second thresholding condition $|\mathbf{n}| > \hat{n}$ in Eq. (22). Here $\bar{n}$ is a small but finite number.

To obtain an analytical expression for the width of the interface region, Eq. (D14) can be used in the stationary state to estimate that, at the limits of region II, the function h_φ takes the value

$$h_\varphi|_{|\mathbf{n}|=\bar{n}} = \frac{c_S\Delta t}{2\beta\gamma}\bar{n} \tag{E1}$$

instead of the original $h_\varphi = 0$. Using the quadratic form of h_φ given in Eq. (33) and solving Eq. (E1) for the values of φ at

the limits gives

$$\varphi_1 = \alpha_1 - \frac{(\alpha_1 - \alpha_2)c_S \Delta t}{2\beta\gamma}\bar{n}, \tag{E2}$$

$$\varphi_2 = \alpha_2 + \frac{(\alpha_1 - \alpha_2)c_S \Delta t}{2\beta\gamma}\bar{n} \tag{E3}$$

to leading order in the small number $\bar{n}$. The width W of the region is obtained by integrating the stationary balance between the diffusive and antidiffusive fluxes given in Eq. (D14) to obtain

$$\int_{\varphi_2}^{\varphi_1} \frac{d\varphi}{h_\varphi} = \frac{2\beta\gamma}{c_S \Delta t}\int_0^W dx. \tag{E4}$$

Carrying out the integral and using Eqs. (E2) and (E3) gives

$$W = \frac{c_S \Delta t(\alpha_1 - \alpha_2)}{\beta\gamma} \ln\left(\frac{2\beta\gamma}{c_S \Delta t \bar{n}}\right) \tag{E5}$$

to leading order in $\bar{n}$. Table II compares this analytical estimate of the width of the interface to the width measured numerically using the two region II criteria given by Eqs. (19) and (22). Numerically, the finite resolution of the system causes the interface width to become less dependent on $\bar{n}$ as the thresholding value decreases. In practice, to make the interface wider, one must lower the value of β as shown in the table.

TABLE II. Width of region II with $\varphi_{1\text{num}}$ and $\varphi_{2\text{num}}$ being the numerical concentrations just within region I, W_{ana} the analytical width of Eq. (E5), and W_{num} the numerically observed width.

$\bar{n}$	β	α_1	α_2	$\varphi_{1\text{num}}$	$\varphi_{2\text{num}}$	W_{ana}	W_{num}
10^{-2}	1.0	1.0	0.01	0.9991295	0.0101996	5.70	6
10^{-3}	1.0	1.0	0.01	0.9999582	0.0100090	8.23	8
10^{-4}	1.0	1.0	0.01	0.9999981	0.0100090	10.75	9
10^{-2}	1.0	1.0	0.10	0.9996064	0.1000005	5.18	5
10^{-3}	1.0	1.0	0.10	1.0000005	0.1000000	7.48	7
10^{-4}	1.0	1.0	0.10	1.0000005	0.1000000	9.78	7
10^{-3}	0.8	1.0	0.01	0.9997631	0.0100946	9.07	10
10^{-3}	0.6	1.0	0.01	0.9989784	0.0105631	11.62	12
10^{-3}	0.4	1.0	0.01	0.9986830	0.0109073	16.41	18

[1] D. S. Abrams and J. M. Prausnitz, AIChE J. **21**, 116 (1975).
[2] J. S. Rowlinson, J. Stat. Phys. **20**, 197 (1979).
[3] S. Q. Wang and Q. Shi, Macromolecules **26**, 1091 (1993).
[4] M. R. Swift, E. Orlandini, W. R. Osborn, and J. M. Yeomans, Phys. Rev. E **54**, 5041 (1996).
[5] B. T. Nadiga and S. Zaleski, Euro. J. Mech. B, Fluids **15**, 885 (1996).
[6] F. J. Blas and L. F. Vega, J. Chem. Phys. **109**, 7405 (1998).
[7] E. Daz-Herrera, J. Alejandre, G. Ramrez-Santiago, and F. Forstmann, J. Chem. Phys. **110**, 8084 (1999).
[8] S. K. Das, J. Horbach, and K. Binder, J. Chem. Phys. **119**, 1547 (2003).
[9] R. Ledesma-Aguillar, D. Vella, and J. M. Yeomans, Soft Matter **10**, 8267 (2014).
[10] J. W. Cahn and J. E. Hilliard, J. Chem. Phys. **28**, 258 (1958).
[11] A. J. Bray, Adv. Phys. **43**, 357 (1994).
[12] J.-C. Desplat, I. Pagonabarraga, and P. Bladon, Comput. Phys. Commun. **134**, 273 (2001).
[13] D. H. Rothman and S. Zaleski, *Lattice-Gas Cellular Automata: Simple Models of Complex Hydrodynamics* (Cambridge University Press, Cambridge, 1997).
[14] S. Succi, *The Lattice-Boltzmann Equation* (Oxford University Press, Oxford, 2001).
[15] E. G. Flekkøy, Phys. Rev. E **47**, 4247 (1993).
[16] X. Shan and G. Doolen, J. Stat. Phys. **81**, 379 (1995).
[17] M. E. McCracken and J. Abraham, Phys. Rev. E **71**, 046704 (2005).
[18] B. Chopard, J. L. Falcone, and J. Latt, Eur. Phys. J. Spec. Top. **171**, 245 (2009).
[19] S. D. C. Walsh and M. O. Saar, Phys. Rev. E **82**, 066703 (2010).
[20] C. Chen and D. Zhang, Phys. Fluids **21**, 103301 (2009).
[21] A. Hebach, A. Oberhof, N. Dahmen, A. Kögel, H. Ederer, and E. Dinjus, J. Chem. Eng. Data **47**, 1540 (2002).
[22] F. Tewes and F. Boury, J. Phys. Chem. B **108**, 2405 (2004).
[23] U. D'Ortona, D. Salin, M. Cieplak, R. B. Rybka, and J. R. Banavar, Phys. Rev. E **51**, 3718 (1995).
[24] M. Latva-Kokko and D. H. Rothman, Phys. Rev. E **71**, 056702 (2005).
[25] J. U. Brackbill, D. B. Kothe, and C. Zemach, J. Comput. Phys. **100**, 335 (1992).
[26] L. D. Landau and E. M. Lifshitz, *Fluid Mechanics*, 2nd ed. (Butterworth-Heinemann, Oxford, 1987).
[27] Z. Guo, C. Zheng, and B. Shi, Phys. Rev. E **65**, 046308 (2002).
[28] V. A. Bloomfield and R. K. Dewan, J. Phys. Chem. **75**, 3113 (1971).
[29] K. Langaas and J. M. Yeomans, Eur. Phys. J. B **15**, 133 (2000).
[30] R. Scardovelli and S. Zaleski, Annu. Rev. Fluid Mech. **31**, 567 (1999).
[31] A. J. Wagner, Int. J. Mod. Phys. B **17**, 193 (2003).
[32] L. Wu, M. Tsutahara, L. S. Kim, and M. Ha, Int. J. Multiphase Flow **34**, 852 (2008).
[33] J. R. Cannon, *The One-Dimensional Heat Equation* (Cambridge University Press, Cambridge, 1984).
[34] M. Latva-Kokko and D. H. Rothman, Phys. Rev. E **72**, 046701 (2005).
[35] O. Aursjø, H. A. Knudsen, E. G. Flekkøy, and K. J. Måløy, Phys. Rev. E **82**, 026305 (2010).